Enhancing Circular Dichroism Signals with Vector Beams

Lyuzhou Ye[●],[1] Longqing Yang,[1] Xiao Zheng[●],[1,2,*] and Shaul Mukamel[●][3]

[1]*Hefei National Laboratory for Physical Sciences at the Microscale & Synergetic Innovation Center of Quantum Information and Quantum Physics and CAS Center for Excellence in Nanoscience, University of Science and Technology of China, Hefei, Anhui 230026, China*
[2]*Department of Chemical Physics and Key Laboratory of Surface and Interface Chemistry and Energy Catalysis of Anhui Higher Education Institutes, University of Science and Technology of China, Hefei, Anhui 230026, China*
[3]*Department of Chemistry and Department of Physics and Astronomy, University of California, Irvine, California 92697, USA*

Circular dichroism (CD) is broadly employed for distinguishing molecular chiralities. However, its practical application is often limited by the weak magnitude of chiral signal. We propose to use azimuthally and radially polarized vector beams to probe CD spectra. By taking advantage of the strong longitudinal components of the vector beams, the transmitted light can be detected in the radial direction. The resulting CD signal is several orders of magnitude stronger than conventional CD signal with plane waves. Quantitative analysis and numerical simulations show that the enhancement factor is independent of molecular properties and can be increased by decreasing the path length of the sample cuvette and the interaction cross section between the light beam and molecular sample. The proposed novel CD spectroscopy is feasible with the current optical technology.

An object is chiral if it cannot be superimposed on its mirror image. Molecular chirality is of crucial importance in many areas of science and technology, including enantioselective synthesis and catalysis [1,2], molecular spintronics [3,4], and drug design [5,6]. A chiral molecule and its mirror image, known as enantiomers, possess an opposite handedness, which can strongly affect their physical, chemical, and biological properties. Enantiomer discrimination has drawn considerable attention in the applications of molecular chirality.

Since the 19th century, numerous spectroscopic methods have been developed for the accurate and efficient characterization of molecular chirality. Circular dichroism (CD) spectroscopy is one of the most widely used techniques. The CD spectrum is defined as the differential absorption of left- and right-circularly polarized (LCP and RCP) light, and is generally several orders of magnitude weaker than the usual absorption spectrum. This is because the CD signal manifests itself through the interference of the electric and magnetic dipole interactions [7], while the absorption signal is dominated by the much stronger electric dipole interaction with the electric field.

Many methods have been proposed for enhancing the weak chiral signals. An intense laser field interacting with chiral molecules can significantly enhance the chiral-sensitive magnetic-dipole transitions, amplifying subfemtosecond chiral high-harmonic generation spectra [8]. Plasmonic nanostructures [9–12] and chiral metasurfaces [13,14] were fabricated for the ultrasensitive detection and characterization of chiral biomolecules. Very recently, a 500-fold enhancement of circularly polarized emission has been achieved by embedding the molecule in an achiral environment [15]. By reducing the wavelength to the extreme-ultraviolet or x-ray regimes [16], higher-order multipoles may contribute to the CD signals. A new generation of chiral techniques which do not rely on magnetic-dipole transitions have been explored, including chiral microwave three-wave mixing [17,18], photoelectron CD [19–23], and photoexcited CD [24].

There has been an increasing recent interest in utilizing light beams with complex spatial profiles to enhance chiral signals. Tang *et al.* have demonstrated that enhanced chiral asymmetry can be obtained by a superchiral standing wave setup [25,26]. Twisted light beams offer a new degree of freedom, the orbital angular momentum (OAM), in addition to the polarization (spin), that can be used to detect CD and Raman optical activity signals of enantiomers [16,27–30]. A CD spectrum enhanced by a factor of 2 was predicted in the x-ray regime [16].

In addition to the OAM-carrying twisted light, vector beams (VBs) constitute another type of spatially structured light. These are axially symmetric solutions to the vector Helmholtz equation [31,32]. Unlike conventional laser beams which have spatially homogeneous states of polarization (e.g., linear, elliptical, and circular), VBs have inhomogeneous polarization distributions in space. Two

typical VBs are azimuthally (AP) or radially polarized (RP) beams, whereby the polarization of the transverse electric field can be aligned in the azimuthal or radial direction. Various strategies have been developed to generate VBs. Conventional Gaussian beams can be transformed into VBs by specially designed mode converters [33–35]. VBs have led to wide applications in free-space communications [36], biosensors [37], and optical data storage [38]. Of particular interest is the longitudinal component of the VBs. An AP (RP) VB has a strong magnetic (electric) field along the beam axis [39,40]. They have been applied in optical trapping [41], superresolution microscopy [42], and laser micromachining [43]. However, their spectroscopic applications are still scarce [44,45].

In this work, we demonstrate substantial enhancement of CD signals with VBs (VBCD signals). Compared with the Poynting vector used in conventional CD measurements, which only has a longitudinal component, VBs also have transverse (radial and azimuthal) components. Hence, the transmitted light after passing through the sample cuvette can be detected in the radial, azimuthal, or the longitudinal directions. We find that while the signals detected by the latter two are similar to conventional CD, the radial measurements can be enhanced by several orders of magnitude.

VBs have cylindrical symmetry along the beam axis, and are best described with cylindrical coordinates. For brevity, in the following we only present the positive-frequency components of the electric and magnetic fields, $E^{(+)}$ and $B^{(+)}$, while leaving their complex conjugates, $E^{(-)}$ and $B^{(-)}$, to the Supplemental Material [46]. The electric field of the AP VB is given by $E_A^{(+)}(r,t) = \hat{\phi}E(r)e^{i(kz-\omega t)}$, where $\hat{\phi}$ is the azimuthal unit vector, and $r \equiv (\rho, \phi, z)$. We assume a Hermite-Gaussian spatial profile [31] $E(r) = [4\rho/\sqrt{\pi}w^2(z)]e^{-[\rho^2/w^2(z)]}e^{i[k\rho^2/2R(z)]}e^{-2i\arctan(z/z_R)}$, k being the wave vector, w_0 the beam waist, $z_R = \frac{1}{2}kw_0^2$ the Rayleigh length, $w(z) = w_0\sqrt{1 + z^2/z_R^2}$ the beam width, and $R(z) = z + z_R^2/z$ the radius of curvature. The corresponding magnetic field is $B_A^{(+)}(r,t) = \{\hat{\rho}(-k/\omega) + \hat{z}(-i/\omega)[(1/\rho) + (\partial/\partial\rho)]\}E(r)e^{i(kz-\omega t)}$. The electric and magnetic fields of RP VBs are [31] $E_R^{(+)}(r,t) = \{\hat{\rho} + \hat{z}(i/k)[(1/\rho) + (\partial/\partial\rho)]\}E(r)e^{i(kz-\omega t)}$ and $B_R^{(+)}(r,t) = \hat{\phi}(k/\omega)E(r)e^{i(kz-\omega t)}$, respectively. Note that both $B_A^{(+)}$ and $E_R^{(+)}$ have a nonzero longitudinal z component, which can contribute to the transverse components of the Poynting vector.

In analogy to the LCP and RCP plane waves of conventional CD, we propose two complementary beams for realizing the VBCD measurement. These are superpositions of the AP and RP VBs, and are denoted left- and right-circularly polarized beams with nonzero *longitudinal* components (abbreviated as LCPL and RCPL beams), respectively.
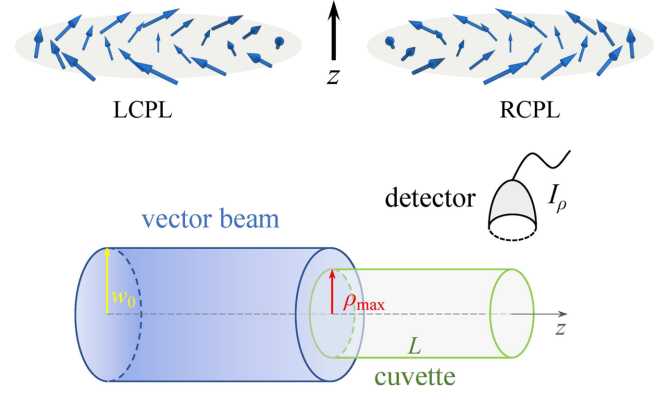

FIG. 1. Top: spatial distributions of the electric fields of the LCPL and RCPL beams. Bottom: experimental setup for detecting the absorption signals in the $\hat{\rho}$ direction $I_\rho(\omega)$. w_0 is the beam waist, L is the path length of the cylindrical sample cuvette, and ρ_{max} is the radius of interaction cross section between the VB and the molecular sample.

$$\begin{pmatrix} E_j^{(+)}(r,t) \\ B_j^{(+)}(r,t) \end{pmatrix} = \frac{-1}{\sqrt{2}} \begin{pmatrix} E_A^{(+)}(r,t) & E_R^{(+)}(r,t) \\ B_A^{(+)}(r,t) & B_R^{(+)}(r,t) \end{pmatrix} \begin{pmatrix} c_j \\ i \end{pmatrix}. \tag{1}$$

Here, $c_j = 1$ for $j = $ LCPL and -1 for $j = $ RCPL. The spatial profiles of the electric fields of these two beams are illustrated in the top panel of Fig. 1, where the field vectors exhibit longitudinal (z) component perpendicular to the transverse plane.

The light-matter interaction is described by the semi-classical Hamiltonian $H_{int}(t) = -\hat{\mu} \cdot E(r,t) - \hat{m} \cdot B(r,t) - \frac{1}{2}\hat{Q}:\nabla E(r,t)$, where $\hat{\mu}$, $\hat{m}$, and $\hat{Q}$ are the electric dipole, magnetic dipole, and electric quadrupole operators, respectively, and E and B are given by the real parts of $E^{(+)}$ and $B^{(+)}$, respectively. For randomly oriented molecules in the gas phase or in solution, the electric quadrupole contribution to the signal vanishes upon rotational averaging [49]. Using the first-order time-dependent perturbation theory [50], the wave vectors $k_j(\omega)$ in the paraxial approximation satisfy

$$k_j^2 - \frac{\omega^2}{c^2} - n_0\mu_0\omega^2\chi_{\mu\mu}(\omega) - 2ic_j n_0\mu_0\omega k_j\chi_{\mu m}(\omega)$$
$$- n_0\mu_0 k_j^2\chi_{mm}(\omega) = 0. \tag{2}$$

Here, c is the speed of light, μ_0 is the magnetic permeability, and n_0 is the molecular number density. The rotationally averaged electric or magnetic susceptibility tensor is expressed in the sum-over-states form as $\chi_{\alpha\beta}(\omega) = \sum_n[(\beta_{gn}\alpha_{ng})/(\omega + \omega_{ng} + i\eta) - (\alpha_{gn}\beta_{ng})/(\omega - \omega_{ng} + i\eta)]$, where $\alpha, \beta = \{\mu, m\}$, and g and n denote the ground and the n'th excited state, respectively.

From Eq. (1) it follows that the Poynting vector $I(r)$ is nonzero in the $\hat{\rho}$, $\hat{\phi}$, and $\hat{z}$ directions [46]. The transmitted light can thus be detected in all three directions.

In Fig. 1 we sketch the experimental setup for measuring the ρ component of the Poynting vector $I_\rho(\omega)$. A cylindrical sample cuvette of length L is aligned coaxially with the light beam, and $\rho_{\max}$ is the radius of the interaction cross section between the VBs and the molecular samples. Assuming a large beam waist, the linear absorption signal measured after passing through the sample cuvette is given by

$$I_\rho(\omega; k_j) \simeq \frac{2}{\mu_0 c} e^{-2\mathrm{Im}(k_j)L} \left[\mathrm{Im}\left(\frac{2D}{k_j w_0} - \frac{2w_0 F}{k_j w_0^2 + 2iL} \right) \right], \quad (3)$$

where k_j is obtained by solving Eq. (2). D and F are dimensionless functions of the reduced radius $\gamma_\rho \equiv \rho_{\max}/w_0$, evaluated as $D(\gamma_\rho) \equiv w_0 \int_0^{\rho_{\max}} d\rho |E(r)|^2$ and $F(\gamma_\rho) \equiv w_0^{-1} \int_0^{\rho_{\max}} d\rho \rho^2 |E(r)|^2$ [46]. Note that the square-bracketed term in Eq. (3) comes from the longitudinal component of the VBs. The linear absorption signal for plane waves is recovered by setting this term to 1.

The absorption spectrum of light beam j ($j = $ LCPL, RCPL) is given by $\epsilon_\rho(\omega; k_j) = (n_0 L)^{-1} \ln(I_\rho(\omega; k_0)/I_\rho(\omega; k_j))$, where $k_0 = \omega/c$ is the wave vector in vacuum. The CD spectrum detected in the $\hat{\rho}$ direction is

$$\Delta\epsilon_\rho(\omega) \equiv \epsilon_\rho(\omega; k_{\mathrm{LCPL}}) - \epsilon_\rho(\omega; k_{\mathrm{RCPL}})$$
$$\simeq \frac{2\mathrm{Im}(\Delta k)}{n_0} \left[1 + \left(\frac{1}{2\gamma_L} \right)^2 \left(\frac{D}{F} - 1 \right) \right], \quad (4)$$

where $\Delta k \equiv k_{\mathrm{LCPL}} - k_{\mathrm{RCPL}}$, and $\gamma_L \equiv L/w_0$ is the reduced path length. $\mathrm{Im}(\Delta k)$ is proportional to the (rotationally averaged) rotatory strength $\mathrm{Im}(\mu_{gn} m_{ng})$ of transitions between the ground state and excited states, which represents the molecular chirality.

The CD spectrum with VBs measured along $\hat{z}$ ($\Delta\epsilon_z$) is found to be close to that obtained with plane waves ($\Delta\epsilon_{\mathrm{PW}}$), given by $\Delta\epsilon_z(\omega) \simeq \Delta\epsilon_{\mathrm{PW}}(\omega) \simeq [2\mathrm{Im}(\Delta k)/n_0]$. Comparison with Eq. (4) shows that in addition to the standard plane-wave term, $\Delta\epsilon_\rho$ has an extra enhancement factor originating from the longitudinal component of the VBs.

We emphasize that the molecular properties (e.g., the electric and magnetic dipoles) are solely included in the factor $\mathrm{Im}(\Delta k)$ of Eq. (4), which is the same as in conventional CD. The enhancement factor given by the square-bracketed term in Eq. (4) is completely determined by two dimensionless parameters: the reduced path length γ_L and the reduced radius γ_ρ, which are independent of the molecular properties. Thus the proposed CD technique ($\Delta\epsilon_\rho$) carries the same spectroscopic information as conventional CD ($\Delta\epsilon_{\mathrm{PW}}$), but contains an additional enhancement factor.
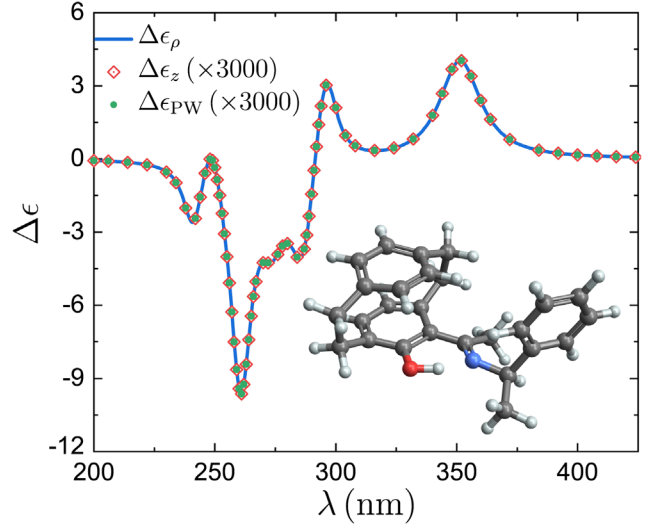

FIG. 2. The simulated CD spectra with VBs ($\Delta\epsilon_\rho$ and $\Delta\epsilon_z$) and plane waves ($\Delta\epsilon_{\mathrm{PW}}$). The parameters used are the beam waist $w_0 = 1$ mm, the radius of the interaction cross section $\rho_{\max} = 1$ mm, and the path length $L = 10$ μm. The light beam frequency ω has been converted to wavelength $\lambda = 2\pi c/\omega$. The inset shows the molecular structure of (R_p,R)-5-(methyl(1-(phenyl)ethylimino)methyl)-4-hydroxy(2.2)paracyclophane. All quantum chemistry calculations are carried out by using the ORCA program [52]. Computational details are given in the Supplemental Material [46].

To demonstrate the strong enhancement of $\Delta\epsilon_\rho$, we have simulated the CD spectrum of (R_p,R)-5-(methyl(1-(phenyl)ethylimino)methyl)-4-hydroxy(2.2)paracyclophane (see the inset of Fig. 2). This molecule offers a versatile tool for asymmetric carbon-carbon bond forming reactions [51].

The absorption and CD signal simulations depicted in Fig. 2 employ experimentally realistic parameters: the radius of the interaction cross section is taken to be equal to the beam waist $\rho_{\max} = w_0 = 1$ mm, and the path length is set to $L = 10$ μm. As expected from Eq. (4), while the line shape of $\Delta\epsilon_\rho$ is almost identical to $\Delta\epsilon_z$ and $\Delta\epsilon_{\mathrm{PW}}$, its intensity is amplified by a factor of 3000.

The reduced path length γ_L and the reduced radius γ_ρ of the interaction cross section are the key parameters that determine the enhancement factor of VBCD. In Fig. 3 we examine the variation of the enhancement of CD signal intensity $\Delta\epsilon_\rho/\Delta\epsilon_{\mathrm{PW}}$ with γ_L and γ_ρ, with the beam wavelength held at $\lambda = 260.8$ nm. Such enhancement originates from the radial distribution of the longitudinal components of LCPL and RCPL beams.

The enhancement is more pronounced as for lower γ_L and γ_ρ, and the enhancement factor can be as high as 10^6 with the proper choice of L and $\rho_{\max}$. This can be explained by referring to Eq. (4). The ratio D/F monotonically decreases with γ_ρ, and $\lim_{\gamma_\rho \to \infty}(D/F) = (4/3)$ [46]. This guarantees the positivity of the enhancement factor, implying that the radially detected CD signal $\Delta\epsilon_\rho$ is always
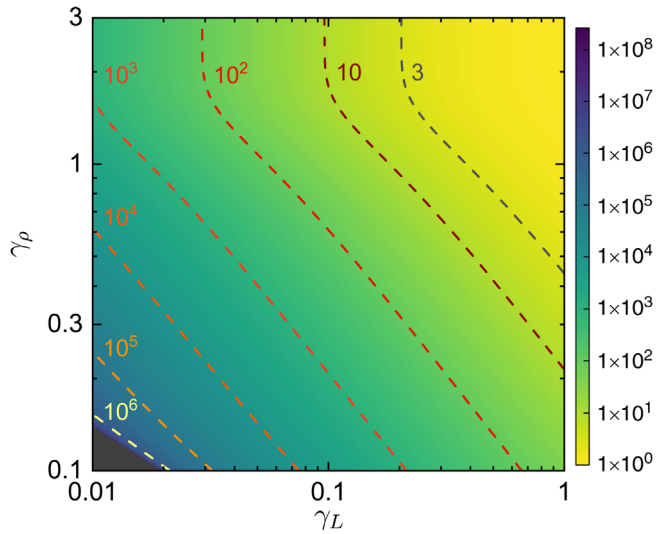
FIG. 3. The enhancement of CD signal intensity $\Delta\epsilon_\rho/\Delta\epsilon_{PW}$ as a function of the reduced path length γ_L and the reduced radius γ_ρ of interaction cross section. The beam waist is $w_0 = 1$ mm. The beam wavelength is held at $\lambda = 260.8$ nm. The discussion of the small shaded region in the lower left-hand corner is given in the main text.

stronger than the conventional CD $\Delta\epsilon_{PW}$. When $\gamma_\rho > 2$, the variation of the enhancement factor with γ_ρ is inconspicuous at a given γ_L. This is because almost all the energy of the light is confined in this region for the Hermite-Gaussian beam profile, and further increasing γ_ρ does not bring about any tangible changes. Moreover, the enhancement factor scales inverse quadratically with sample cuvette path length L. Hence, a small L would substantially magnify the CD signal $\Delta\epsilon_\rho$.

We note that when the γ_L and γ_ρ are very small (the shaded region in the lower left-hand corner in Fig. 3), $I_\rho(\omega; k_i)$ is negative, implying that the ρ component of the Poynting vector points in the negative radial direction. Thus, the equation of $\epsilon_\rho(\omega; k_j)$ is no longer applicable, and the light in this case cannot be effectively detected. Nevertheless, this is a rather small parameter region compared with the rest of plot.

Based on the above analysis, strongly enhanced CD signals can be achieved by increasing the beam waist, decreasing the interaction cross section, or decreasing the path length of the sample cuvette. In experimental CD spectroscopy of biological molecules, the beam waist and path length vary between a few microns to millimeters [53]. The AP and RP VBs can be readily generated by using designed optical elements [35]. Hence, our proposed method for enhancing the CD signals is well within the reach of current technology.

To conclude, we have proposed a novel VBCD technique for enhancing CD signals. The transmitted light beams given by superposition of AP and RP VBs are detected in the radial direction, and the VBCD signal is found to be markedly stronger than conventional CD, thanks to the strong longitudinal component of the VBs. The enhancement factor given by Eq. (4) is independent of molecular properties, but is solely determined by the path length L of sample cuvette and the radius ρ_{max} of interaction cross section between the light beam and molecular samples. Numerical simulations of the CD signals of a paracyclophane molecule quantify the enhancement effect as a function of γ_L and γ_ρ.

VBCD can be used to enhance the CD spectrum, which is the simplest and most widely used spectroscopic probe of molecular chirality. We expect that the enhancement factor can be further increased by designing VBs with more complicated spatial profiles [54]. Furthermore, VBs can be employed for other chirality-sensitive spectroscopies, such as optical rotatory dispersion, time-resolved CD, optical Raman activity, and photoelectron CD, by taking advantage of the strong longitudinal components of the light beams.

---

[*] xz58@ustc.edu.cn

[1] P. Melchiorre, M. Marigo, A. Carlone, and G. Bartoli, Angew. Chem. Int. Ed. **47,** 6138 (2008).

[2] J. Pan, J.-H. Wu, H. Zhang, X. Ren, J.-P. Tan, L. Zhu, H.-S. Zhang, C. Jiang, and T. Wang, Angew. Chem., Int. Ed. **131,** 7503 (2019).

[3] B. Göhler, V. Hamelbeck, T. Markus, M. Kettner, G. Hanne, Z. Vager, R. Naaman, and H. Zacharias, Science **331,** 894 (2011).

[4] M. Suda, Y. Thathong, V. Promarak, H. Kojima, M. Nakamura, T. Shiraogawa, M. Ehara, and H. M. Yamamoto, Nat. Commun. **10,** 2455 (2019).

[5] M. D. Eastgate, M. A. Schmidt, and K. R. Fandrick, Nat. Rev. Chem. **1,** 0016 (2017).

[6] M. Patel, R. Kumar, K. Kishor, T. Mlsna, C. U. Pittman, Jr., and D. Mohan, Chem. Rev. **119,** 3510 (2019).

[7] E. Power and T. Thirunamachandran, J. Chem. Phys. **60,** 3695 (1974).

[8] R. Cireasa, A. Boguslavskiy, B. Pons, M. Wong, D. Descamps, S. Petit, H. Ruf, N. Thiré, A. Ferré, J. Suarez, J. Higuet, B. Schmidt, A. Alharbi, F. Légaré, V. Blanchet, B. Fabre, S. Patchkovskii, O. Smirnova, Y. Mairesse, and V. Bhardwaj, Nat. Phys. **11,** 654 (2015).

[9] A. Kuzyk, R. Schreiber, Z. Fan, G. Pardatscher, E.-M. Roller, A. Högele, F. C. Simmel, A. O. Govorov, and T. Liedl, Nature (London) **483**, 311 (2012).

[10] X. Zambrana-Puyalto, X. Vidal, and G. Molina-Terriza, Nat. Commun. **5**, 4922 (2014).

[11] M. Hentschel, M. Schäferling, X. Duan, H. Giessen, and N. Liu, Sci. Adv. **3**, e1602735 (2017).

[12] M. Hanifeh, M. Albooyeh, and F. Capolino, ACS Photonics **7**, 2682 (2020).

[13] E. Hendry, T. Carpy, J. Johnston, M. Popland, R. Mikhaylovskiy, A. Lapthorn, S. Kelly, L. Barron, N. Gadegaard, and M. Kadodwala, Nat. Nanotechnol. **5**, 783 (2010).

[14] R. Tullius, A. S. Karimullah, M. Rodier, B. Fitzpatrick, N. Gadegaard, L. D. Barron, V. M. Rotello, G. Cooke, A. Lapthorn, and M. Kadodwala, J. Am. Chem. Soc. **137**, 8380 (2015).

[15] J. Wade, J. R. Brandt, D. Reger, F. Zinna, K. Y. Amsharov, N. Jux, D. L. Andrews, and M. J. Fuchter, Angew. Chem., Int. Ed. **133**, 224 (2021).

[16] L. Ye, J. R. Rouxel, S. Asban, B. Rösner, and S. Mukamel, J. Chem. Theory Comput. **15**, 4180 (2019).

[17] D. Patterson, M. Schnell, and J. M. Doyle, Nature (London) **497**, 475 (2013).

[18] D. Patterson and J. M. Doyle, Phys. Rev. Lett. **111**, 023008 (2013).

[19] C. Westphal, J. Bansmann, M. Getzlaff, and G. Schönhense, Phys. Rev. Lett. **63**, 151 (1989).

[20] N. Böwering, T. Lischke, B. Schmidtke, N. Müller, T. Khalil, and U. Heinzmann, Phys. Rev. Lett. **86**, 1187 (2001).

[21] D. Catone, M. Stener, P. Decleva, G. Contini, N. Zema, T. Prosperi, V. Feyer, K. C. Prince, and S. Turchini, Phys. Rev. Lett. **108**, 083001 (2012).

[22] S. Beaulieu, A. Comby, A. Clergerie, J. Caillat, D. Descamps, N. Dudovich, B. Fabre, R. Géneaux, F. Légaré, S. Petit, B. Pons, G. Porat, T. Ruchon, R. Taïeb, V. Blanchet, and Y. Mairesse, Science **358**, 1288 (2017).

[23] R. E. Goetz, C. P. Koch, and L. Greenman, Phys. Rev. Lett. **122**, 013204 (2019).

[24] S. Beaulieu, A. Comby, D. Descamps, B. Fabre, G. A. Garcia, R. Géneaux, A. G. Harvey, F. Légaré, Z. Mašín, L. Nahon, A. F. Ordonez, S. Petit, B. Pons, Y. Mairesse, O. Smirnova, and V. Blanchet, Nat. Phys. **14**, 484 (2018).

[25] Y. Tang and A. E. Cohen, Phys. Rev. Lett. **104**, 163901 (2010).

[26] Y. Tang and A. E. Cohen, Science **332**, 333 (2011).

[27] W. Brullot, M. K. Vanbel, T. Swusten, and T. Verbiest, Sci. Adv. **2**, e1501349 (2016).

[28] K. A. Forbes and D. L. Andrews, Opt. Lett. **43**, 435 (2018).

[29] K. A. Forbes, Phys. Rev. Lett. **122**, 103201 (2019).

[30] K. A. Forbes and D. L. Andrews, Phys. Rev. Research **1**, 033080 (2019).

[31] Q. Zhan, Adv. Opt. Photonics **1**, 1 (2009).

[32] U. Levy, Y. Silberberg, and N. Davidson, Adv. Opt. Photonics **11**, 828 (2019).

[33] G. Machavariani, Y. Lumer, I. Moshe, A. Meir, and S. Jackel, Opt. Lett. **32**, 1468 (2007).

[34] F. Yue, D. Wen, J. Xin, B. D. Gerardot, J. Li, and X. Chen, ACS Photonics **3**, 1558 (2016).

[35] S. Liu, S. Qi, Y. Zhang, P. Li, D. Wu, L. Han, and J. Zhao, Photonics Res. **6**, 228 (2018).

[36] V. D'ambrosio, E. Nagali, S. P. Walborn, L. Aolita, S. Slussarenko, L. Marrucci, and F. Sciarrino, Nat. Commun. **3**, 1 (2012).

[37] R. Wang, L. Du, C. Zhang, Z. Man, Y. Wang, S. Wei, C. Min, S. Zhu, and X.-C. Yuan, Opt. Lett. **38**, 4770 (2013).

[38] Y. Zhang and J. Bai, Opt. Express **17**, 3698 (2009).

[39] L. Novotny, M. R. Beversluis, K. S. Youngworth, and T. G. Brown, Phys. Rev. Lett. **86**, 5251 (2001).

[40] R. Dorn, S. Quabis, and G. Leuchs, Phys. Rev. Lett. **91**, 233901 (2003).

[41] S. Roy, K. Ushakova, Q. van den Berg, S. F. Pereira, and H. P. Urbach, Phys. Rev. Lett. **114**, 103903 (2015).

[42] M. Neugebauer, P. Woźniak, A. Bag, G. Leuchs, and P. Banzer, Nat. Commun. **7**, 11286 (2016).

[43] C. Hnatovsky, V. Shvedov, W. Krolikowski, and A. Rode, Phys. Rev. Lett. **106**, 123901 (2011).

[44] M. Kamandi, M. Albooyeh, M. Veysi, M. Rajaei, J. Zeng, H. K. Wickramasinghe, and F. Capolino, ACS Photonics **5**, 4360 (2018).

[45] F. Graf, J. Feis, X. Garcia-Santiago, M. Wegener, C. Rockstuhl, and I. Fernandez-Corbaton, ACS Photonics **6**, 482 (2019).

[46] See Supplemental Material at http://link.aps.org/supplemental/10.1103/PhysRevLett.126.123001 for more details about vector beams, CD spectra, and quantum chemistry calculations, which includes Refs. [47,48].

[47] J. P. Perdew, M. Ernzerhof, and K. Burke, J. Chem. Phys. **105**, 9982 (1996).

[48] A. Schäfer, H. Horn, and R. Ahlrichs, J. Chem. Phys. **97**, 2571 (1992).

[49] M. Cho, Two-Dimensional Optical Spectroscopy (CRC Press, Boca Raton, FL, 2009).

[50] S. Mukamel, Principles of Nonlinear Optical Spectroscopy (Oxford University Press, New York, 1995).

[51] L. Pu and H.-B. Yu, Chem. Rev. **101**, 757 (2001).

[52] F. Neese, WIREs Comput. Mol. Sci. **2**, 73 (2012).

[53] N. Berova, P. L. Polavarapu, K. Nakanishi, and R. W. Woody, Comprehensive Chiroptical Spectroscopy: Instrumentation, Methodologies, and Theoretical Simulations (John Wiley & Sons, New York, 2011), Vol. 1.

[54] M. Veysi, C. Guclu, and F. Capolino, J. Opt. Soc. Am. B **32**, 345 (2015).

Supplementary Material for

Enhancing circular dichroism signals with vector beams

Lyuzhou Ye,[1] Longqing Yang,[1] Xiao Zheng,[1,2,*] and Shaul Mukamel[3]

[1] *Hefei National Laboratory for Physical Sciences at the Microscale & Synergetic Innovation Center of Quantum Information and Quantum Physics & CAS center for Excellence in Nanoscience, University of Science and Technology of China, Hefei, Anhui 230026, China*
[2] *Department of Chemical Physics & Key Laboratory of Surface and Interface Chemistry and Energy Catalysis of Anhui Higher Education Institutes, University of Science and Technology of China, Hefei, Anhui 230026, China*
[3] *Department of Chemistry and Department of Physics and Astronomy, University of California, Irvine, CA 92697, USA*

(Dated: January 5, 2021)

CONTENTS

A. Derivations of the CD spectra

Using Eq. (1) of the main text, the electric and magnetic fields for vector beams (VBs) are

$$\boldsymbol{E}_j^{(+)}(\boldsymbol{r},t) = \left[\hat{\boldsymbol{\rho}}\frac{-i}{\sqrt{2}} + \hat{\boldsymbol{\phi}}\frac{-c_j}{\sqrt{2}} + \hat{\boldsymbol{z}}\frac{1}{\sqrt{2}k}\left(\frac{1}{\rho} + \frac{\partial}{\partial\rho}\right)\right]E(\boldsymbol{r})e^{i(kz-\omega t)}, \tag{S1}$$

$$\boldsymbol{B}_j^{(+)}(\boldsymbol{r},t) = \left[\hat{\boldsymbol{\rho}}\frac{c_j k}{\sqrt{2}\omega} + \hat{\boldsymbol{\phi}}\frac{-ik}{\sqrt{2}\omega} + \hat{\boldsymbol{z}}\frac{ic_j}{\sqrt{2}\omega}\left(\frac{1}{\rho} + \frac{\partial}{\partial\rho}\right)\right]E(\boldsymbol{r})e^{i(kz-\omega t)}. \tag{S2}$$

Here, the coefficient $c_j = 1$ for $j = $ LCPL and -1 for $j = $ RCPL; see the main text. The time-averaged Poynting vector ($j = $ LCPL and RCPL) is

$$\boldsymbol{I}(\omega,\boldsymbol{r};k_j) = \frac{1}{\mu_0}\frac{1}{T}\int_0^{T=\frac{2\pi}{\omega}} dt\, \boldsymbol{E}_j^{(+)}(\boldsymbol{r},t) \times \boldsymbol{B}_j^{(-)}(\boldsymbol{r},t) + \text{c.c.}, \tag{S3}$$

where, $\boldsymbol{B}_j^{(-)}(\boldsymbol{r},t) = \left[\boldsymbol{B}_j^{(+)}(\boldsymbol{r},t)\right]^*$. Its ρ-component is

$$I_\rho(\omega,\boldsymbol{r};k_j) = \frac{1}{\mu_0}\left[E_{j,\phi}^{(+)}(\boldsymbol{r},t)B_{j,z}^{(-)}(\boldsymbol{r},t) - E_{j,z}^{(+)}(\boldsymbol{r},t)B_{j,\phi}^{(-)}(\boldsymbol{r},t)\right] + \text{c.c.} \tag{S4}$$

$$= \frac{1}{\mu_0}\frac{2\text{Re}(k_j)}{\omega}|E(\boldsymbol{r})|^2 e^{-2\text{Im}(k_j)z}\text{Im}\left(\frac{2}{k_j\rho} - \frac{2\rho}{k_j w_0^2 + 2iz}\right). \tag{S5}$$

Here, $E_{j,\zeta}^{(\pm)}$ and $B_{j,\zeta}^{(\pm)}$ with $\zeta = \{\phi, z\}$ are the ζ-component of the electric and magnetic fields, respectively. After passing through the sample cuvette of length L, the absorption signal for beam j measured in $\hat{\boldsymbol{\rho}}$-direction is

$$I_\rho(\omega;k_j) = \int_0^{\rho_{\max}} d\rho\, \rho I_\rho(\omega,\boldsymbol{r};k_j) \simeq \frac{2}{\mu_0 c}e^{-2\text{Im}(k_j)L}\text{Im}\left(\frac{2D}{k_j w_0} - \frac{2w_0 F}{k_j w_0^2 + 2iL}\right), \tag{S6}$$

where $\rho_{\max}$ is the radius of interaction cross section between the beam and the molecular sample; see Fig. (1) of the main text. By assuming a large beam waist w_0 ($\sim 1\,\text{mm}$), we have $w(z) \simeq w_0$ and $e^{i\frac{k\rho^2}{2R(z)}}e^{-2i\arctan(z/z_R)} \simeq 1$; see the main text for details. Then the two dimensionless functions D and F can be obtained by evaluating the two integrals

$$\int_0^{\rho_{\max}} d\rho\, |E(\boldsymbol{r})|^2 \simeq w_0^{-1}\left[\sqrt{\frac{2}{\pi}}\text{erf}\left(\sqrt{2}\gamma_\rho\right) - \frac{4}{\pi}\gamma_\rho e^{-2\gamma_\rho^2}\right] \equiv w_0^{-1}D(\gamma_\rho), \tag{S7}$$

and

$$\int_0^{\rho_{\max}} d\rho\, \rho^2 |E(\boldsymbol{r})|^2 \simeq w_0\left[\frac{3}{2\sqrt{2\pi}}\text{erf}\left(\sqrt{2}\gamma_\rho\right) - \frac{1}{\pi}\gamma_\rho e^{-2\gamma_\rho^2}\left(3 + 4\gamma_\rho^2\right)\right] \equiv w_0 F(\gamma_\rho), \tag{S8}$$

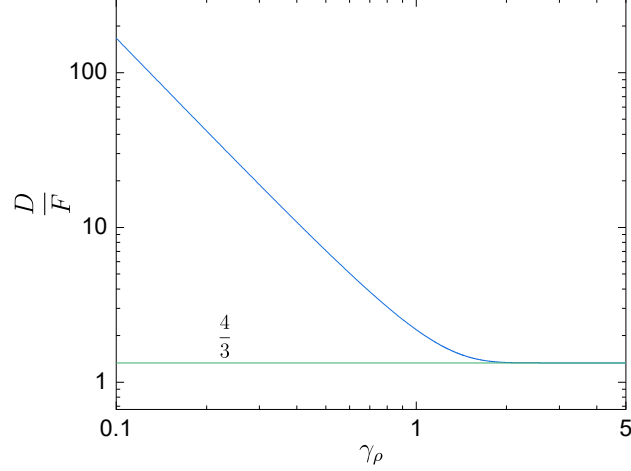where $\gamma_\rho \equiv \frac{\rho_{\max}}{w_0}$ is the reduced radius of the interaction cross section.

FIG. S1. The variation of $\frac{D}{F}$ with the reduced radius γ_ρ.

The CD spectrum detected in the $\hat{\boldsymbol{\rho}}$-direction is (see the main text for the definition of the absorption spectrum ϵ_ρ)

$$\Delta\epsilon_\rho(\omega) = \epsilon_\rho(\omega; k_{\mathrm{LCPL}}) - \epsilon_\rho(\omega; k_{\mathrm{RCPL}}) \tag{S9}$$

$$= \frac{1}{n_0 L} \ln \frac{I_\rho(\omega; k_{\mathrm{RCPL}})}{I_\rho(\omega; k_{\mathrm{LCPL}})} \tag{S10}$$

$$\simeq \frac{2\mathrm{Im}(\Delta k)}{n_0} + \frac{1}{n_0 L} \left\{ \frac{\mathrm{Im}\left(\frac{D}{k_{\mathrm{RCPL}}} - \frac{F}{k_{\mathrm{RCPL}} + \frac{2iL}{w_0^2}}\right)}{\mathrm{Im}\left(\frac{D}{k_{\mathrm{LCPL}}} - \frac{F}{k_{\mathrm{LCPL}} + \frac{2iL}{w_0^2}}\right)} - 1 \right\} \tag{S11}$$

$$\simeq \frac{2\mathrm{Im}(\Delta k)}{n_0} + \frac{1}{n_0 L} \left\{ \frac{\mathrm{Im}\left(\frac{D}{k_{\mathrm{RCPL}}} - \frac{F\left(k_{\mathrm{RCPL}}^* - \frac{2iL}{w_0^2}\right)}{|k_{\mathrm{RCPL}}|^2}\right)}{\mathrm{Im}\left(\frac{D}{k_{\mathrm{LCPL}}} - \frac{F\left(k_{\mathrm{LCPL}}^* - \frac{2iL}{w_0^2}\right)}{|k_{\mathrm{LCPL}}|^2}\right)} - 1 \right\} \tag{S12}$$

$$\simeq \frac{2\mathrm{Im}(\Delta k)}{n_0} + \frac{1}{n_0 L} \left\{ \frac{(F-D)\mathrm{Im}\left(k_{\mathrm{RCPL}}\right) + \frac{2L}{w_0^2}F}{(F-D)\mathrm{Im}\left(k_{\mathrm{LCPL}}\right) + \frac{2L}{w_0^2}F} - 1 \right\} \tag{S13}$$

$$\simeq \frac{2\mathrm{Im}(\Delta k)}{n_0} \left[1 + \left(\frac{1}{2\gamma_L}\right)^2 \left(\frac{D}{F} - 1\right) \right], \tag{S14}$$

where we define $\Delta k(\omega) \equiv k_{\mathrm{LCPL}}(\omega) - k_{\mathrm{RCPL}}(\omega)$. Using the expressions in Eqs. (S7) and (S8), we show in Fig. S1 that the ratio $\frac{D}{F}$ monotonically decreases with γ_ρ, and $\lim_{\gamma_\rho \to \infty} \frac{D}{F} = \frac{4}{3}$.

Similar to the derivations of Eqs. (S4)–(S6), the absorption signal for beam j measured in $\hat{\boldsymbol{z}}$-direction is

$$I_z(\omega; k_j) \simeq \frac{2}{\mu_0 c} e^{-2\mathrm{Im}(k_j)L} \frac{2}{\pi} \left[1 - e^{-2\gamma_\rho^2} \left(1 + 2\gamma_\rho^2\right) \right]. \tag{S15}$$

Then the CD spectrum detected in the $\hat{z}$-direction is

$$\Delta\epsilon_z(\omega) = \epsilon_z(\omega; k_{\mathrm{LCPL}}) - \epsilon_z(\omega; k_{\mathrm{RCPL}}) \tag{S16}$$

$$= \frac{1}{n_0 L} \ln \frac{I_z(\omega; k_{\mathrm{RCPL}})}{I_z(\omega; k_{\mathrm{LCPL}})} \tag{S17}$$

$$\simeq \frac{2\mathrm{Im}(\Delta k)}{n_0}, \tag{S18}$$

which is the same as the conventional CD spectrum with plane waves. This is also verified by the numerical simulations in Fig. (2) of the main text.

B. Details of quantum chemistry calculations

The quantum chemistry calculations are performed by using ORCA program [1]. The geometry of (R_{p},R)-5-(methyl(1-(phenyl)ethylimino)methyl)-4-hydroxy(2.2)paracyclophane molecule is optimized in toluene using density functional theory (DFT) with the hybrid density functional of Perdew, Burke, and the Enzerhof (PBE0) [2] and Karlsruhe split valence plus polarization (SVP) [3] basis sets. The fifteen lowest excited electronic states are calculated in toluene using the time-dependent DFT at the PBE0/SVP level. The conductor-like polarizable continuum model (CPCM) is used to account for the solvent effects for both the structure optimization and excited-state calculation. Table S1 gives the optimized Cartesian atomic coordinates of the molecule in toluene. Table S2 shows the TDDFT calculated energies, electric and magnetic dipoles of the fifteen lowest excited states of the molecule.

TABLE S1: Optimized Cartesian coordinates x, y, z (in units of Å) of (R_{p},R)-5-(methyl(1-(phenyl)ethylimino)methyl)-4-hydroxy(2.2)paracyclophane in toluene.

Atom	x (Å)	y (Å)	z (Å)
C	1.336011	−0.024870	3.227314
C	0.051936	0.450684	3.563760
C	−0.620638	−0.133820	4.653275
C	−0.026104	−1.168552	5.393508
C	1.250576	−1.635128	5.049442
C	1.930163	−1.059558	3.963223
C	−0.588127	1.597479	2.775897
N	−0.522710	1.335731	1.331943
C	−1.406840	0.609833	0.693631
C	−2.604417	0.001148	1.399179
C	−1.269029	0.488029	−0.772189
C	−1.895481	−0.549884	−1.543993
C	−1.963494	−0.381962	−2.933121
C	−1.196556	0.598352	−3.592447
C	−0.303708	1.407559	−2.887005

Atom	x (Å)	y (Å)	z (Å)
C	−0.415362	1.419298	−1.466291
C	−2.133236	−1.965761	−1.022717
C	−0.773239	−2.762728	−0.736341
C	0.429010	−2.166957	−1.445510
C	0.564793	−2.220635	−2.848075
C	1.317121	−1.252929	−3.527699
C	1.954608	−0.206751	−2.828024
C	2.064942	−0.344635	−1.430111
C	1.304307	−1.307264	−0.751012
O	0.372266	2.269459	−0.796948
C	0.901075	2.051552	−3.544872
C	2.218619	1.126184	−3.500042
H	−0.584956	−2.759748	0.351970
H	−0.945224	−3.813146	−1.033048
H	−2.694154	−2.511639	−1.800616
H	−2.739350	−2.017775	−0.105582
H	0.217165	2.031691	0.215082
H	−1.176933	0.608963	−4.689816
H	−2.480802	−1.139155	−3.534200
H	1.136378	3.007160	−3.049710
H	0.667215	2.268379	−4.600439
H	2.562332	0.976033	−4.538191
H	3.011825	1.673382	−2.963411
H	1.290768	−1.230499	−4.624802
H	−0.029759	−2.938431	−3.426862
H	1.289748	−1.299755	0.346420
H	2.622278	0.403312	−0.854164
H	−2.320188	−0.910194	1.955595
H	−3.408496	−0.243216	0.692386
H	−3.002065	0.714289	2.141407
H	−1.621305	0.222661	4.925174
H	−0.564619	−1.612135	6.238257
H	1.714873	−2.445036	5.622667
H	2.927878	−1.418498	3.688457
H	1.868090	0.417547	2.378431
C	0.100071	2.944392	3.063215
H	−1.641611	1.675197	3.107531
H	1.163365	2.909079	2.769364
H	−0.393090	3.750879	2.493294
H	0.043404	3.183975	4.138721

TABLE S2. Information of the fifteen excited states of (R_p,R)-5-(methyl(1-(phenyl)ethylimino)methyl)-4-hydroxy(2.2)paracyclophane in toluene. The energies are in unit of wavenumeber (cm^{-1}). The electric (μ) and magnetic (m) dipoles are in atomic units.

State	Energy (cm^{-1})	μ_x (au)	μ_y (au)	μ_z (au)	m_x (au)	m_y (au)	m_z (au)
1	28344.5	0.25888	0.33214	−0.88321	−0.06201	−0.37491	−0.23738
2	28662.5	0.04132	−0.04137	0.55168	0.24254	0.32027	0.06918
3	33627.5	−0.27139	−0.39018	−0.67661	−0.28008	−0.23773	0.07567
4	34900.3	−0.01994	−0.06624	−0.41731	−0.08123	0.01807	0.21466
5	34912.2	−0.06637	0.03115	−0.01115	−0.02834	0.02581	−0.16922
6	36489.1	0.13209	−0.17070	−0.31876	−0.16131	−0.16577	0.17887
7	38359.3	−0.19667	−0.03818	−1.12593	−0.27323	−0.29732	0.20931
8	33598.5	−0.03202	−0.01807	−0.50295	−0.07399	−0.11299	0.06222
9	37464.3	−0.08186	0.00290	−0.23498	0.00007	0.07720	−0.02255
10	40059.4	−0.04410	−0.02416	−0.29589	−0.07922	−0.06451	−0.00146
11	40066.4	0.02088	−0.21118	−0.52080	−0.06786	−0.14482	−0.00848
12	35564.5	−0.04924	−0.01183	0.05422	−0.00065	0.04360	−0.00948
13	41864.4	−0.18762	−0.16941	−0.23761	−0.04434	−0.04640	0.10740
14	35702.7	0.04606	−0.02666	0.01232	0.00842	0.04479	0.07999
15	41443.8	0.07159	0.05565	0.34609	−0.11631	−0.18195	−0.06898

---

* xz58@ustc.edu.cn

[1] F. Neese, WIREs Comput. Mol. Sci. **2**, 73 (2012).

[2] J. P. Perdew, M. Ernzerhof, and K. Burke, J. Chem. Phys. **105**, 9982 (1996).

[3] A. Schäfer, H. Horn, and R. Ahlrichs, J. Chem. Phys. **97**, 2571 (1992).